# Performance evaluation of the new whole-body PET/CT scanner: Discovery ST

Valentino Bettinardi[1], Massimo Danna[1], Annarita Savi[1], Michela Lecchi[2], Isabella Castiglioni[1], Maria Carla Gilardi[1], Helmut Bammer[3], Giovanni Lucignani[2], Ferruccio Fazio[1]

[1] Department of Nuclear Medicine, Scientific Institute H. San Raffaele, University of Milano-Bicocca, INB-CNR, Milan, Italy
[2] Institute of Radiological Sciences, University of Milan, Milan, Italy
[3] GE Medical Systems, Milwaukee, Wisconsin, USA

Received: 7 December 2003 / Accepted: 27 December 2003 / Published online: 10 February 2004


**Abstract.** Characterisation of the physical performance of the new integrated PET/CT system Discovery ST (GE Medical Systems) has been performed following the NEMA NU 2-1994 (N-94) and the NEMA NU 2-2001 (N-01) standards in both 2D and 3D acquisition configuration. The Discovery ST combines a four or eight multislice helical CT scanner with a PET tomograph which consists of 10,080 BGO crystals arranged in 24 rings. The crystal dimensions are 6.3×6.3×30 $mm^3$ and they are organised in blocks of 6×6 crystals, coupled to a single photomultiplier tube with four anodes. The 24 rings of the PET system allow 47 images to be obtained, spaced by 3.27 mm, and covering an axial field of view of 157 mm. The low- and high-energy thresholds are set to 375 and 650 keV, respectively. The coincidence time window is set to 11.7 ns**.** Using the NEMA N-94 standard, the main results were: (1) the average (radial and tangential) transverse spatial resolution (FWHM) at 1, 10 and 20 cm off axis was 6.28 mm, 7.09 mm and 7.45 mm in 2D, and 6.68 mm, 7.72 mm and 8.13 mm in 3D; (2) the sensitivity for true events was 8,567 cps/kBq/cc in 2D and 36,649 cps/kBq/cc in 3D; (3) the scatter fraction was 15% in 2D and 30% in 3D; (4) the peak true events rate, the true events rate at 50% of the system dead-time and the true events rate when equal to the random events rate were 750 kcps at 189.81 kBq/cc, 744 kcps at 186.48 kBq/cc and 686 kcps at 150.59 kBq/cc, respectively, in 2D, and 922 kcps at 44.03 kBq/cc, 834 kcps at 53.28 kBq/cc and 921 kcps at 44.03 kBq/cc in 3D; (5) the noise equivalent count (NEC) peak rate was 270 kcps at 34.38 kBq/cc in 3D, with random coincidences estimated by delayed events. Using the NEMA N-01 standards the main results were: (1) the average transverse and axial spatial resolution (FWHM) at 1 cm and 10 cm off axis was 6.28 (4.56) mm and 6.88 (6.11) mm in 2D, and 6.29 (5.68) mm and 6.82 (6.05) mm in 3D; (2) the average sensitivity for the two radial positions ($r$=0 cm and $r$=10 cm) was 1.93 cps/kBq in 2D and 9.12 cps/kBq in 3D; (3) the scatter fraction was 19% in 2D and 45% in 3D; (4) the NEC peak rate was 54 kcps at 46.99 kBq/cc in 2D and 45.5 kcps at 10.84 kBq/cc in 3D, when random coincidences were estimated by using $k$=2 in the NEC formula, while the NEC peak rate was 81 kcps at 64.43 kBq/cc and 66 kcps at 14.86 kBq/cc in 2D and 3D, respectively, when random coincidences were estimated by using $k$=1 in the NEC formula. The new integrated PET-CT system Discovery ST has good overall performances in both 2D and 3D, with in particular a high sensitivity and a very good 3D NEC response.

*Keywords:* PET/CT – Discovery ST – Sensitivity – Spatial resolution – NEC response

**Eur J Nucl Med Mol Imaging (2004) 31:867–881**
DOI 10.1007/s00259-003-1444-2

Valentino Bettinardi (✉)
Department of Nuclear Medicine,
Scientific Institute H. San Raffaele,
University of Milano-Bicocca, INB-CNR,
Via Olgettina 60, 20132 Milan, Italy
e-mail: bettinardi.valentino@hsr.it
Tel.: +39-02-26433887, Fax: +39-02-26415202

## Introduction

Positron emission tomography (PET) plays an important role in the staging and restaging of cancer [1] by showing the functional activity of neoplasms with respect to normal tissues. Fluorine-18 fluoro-2-deoxyglucose (FDG) PET whole-body studies allow the detection of neoplastic lesions as regions of increased metabolic activity. In these studies, images are characterized by focal areas of high tracer uptake, corresponding to neoplastic lesions, surrounded by a noisy background. The lack of anatomical reference structures and the poor spatial resolution of the PET systems (4–5 mm) make the interpreta-

tion of PET images difficult, even for experienced nuclear medicine physicians. The registration of functional PET to anatomical magnetic resonance imaging (MRI) or X-ray computed tomography (CT) images represents an important, and often necessary, step in the PET image reporting procedure, enabling correct anatomical localisation of the PET lesions [2].

Within this context, integrated PET/CT systems have been developed in the last few years, in order to provide both anatomical and functional images in a single imaging session [3, 4, 5, 6]. A PET/CT system combines a CT and a PET scanner in the same gantry, allowing patients to undergo CT and PET scans without moving from the scanner bed. The resulting CT and PET images are thus acquired in the same spatial reference system, without the need for an a posteriori alignment by the use of co-registration algorithms.

In the PET/CT systems currently available on the market, both CT and PET are state of the art [7]. The CT scanner is in all cases a helical multi-slice system (from 2 up to 16 slices). The PET scanner is based on different crystal types [bismuth germanate (BGO), lutetium oxyorthosilicate (LSO), gadolinium oxyorthosilicate (GSO)] and different detector architecture (blocks of detectors, continuous pixelated detectors).

More recently, the potential of PET/CT imaging in the definition of the target volume in radiotherapy planning has been demonstrated [8]. PET/CT in fact allows the identification of the viable tumour volume with more accuracy than CT alone. The design of PET/CT systems has thus been modified to account for the requirements of this new application, in particular through the following features:

- A larger bore aperture, to allow immobilisation apparatus to be used as during radiotherapy treatment
- An option to use a flat couch, to allow the patient to be re-positioned during the PET/CT scans and radiotherapeutic sessions
- High sensitivity and isotropic resolution, to allow accurate volume definition and quantification

In this work, the physical response of the PET scanner of the new integrated PET/CT system Discovery ST [9, 10], specifically designed for oncological applications, was characterised by National Electrical Manufacturers Association (NEMA) tests. To provide a comprehensive description of the physical performance of the system in both brain and whole-body imaging applications, both the NEMA NU 2-1994 and the NEMA NU 2-2001 procedures were used [11, 12, 13, 14].

## Materials and methods

### Discovery ST (D-ST)

The D-ST (GE Medical Systems) combines a helical multi-slice CT scanner and a newly designed BGO block detector PET tomograph.

The CT scanner in the D-ST is the High Speed Ultra 4 slice CT scanner (upgradeable to 8), which can cover up to 20 mm in a single tube-detector revolution. The detectors of the High Speed Ultra CT tomograph consist of 16 rows of detectors with 912 detector cells per row. The detector material is a polycrystalline ceramic material, which provides very high absorption efficiency and light output. The Hi-light matrix detector ensures high performance response in low-signal conditions, such as occur in typical low-dose protocols used with the integrated PET/CT system.

The PET tomograph is a newly designed multi-ring BGO block detector system. The BGO crystals are arranged in 24 rings. The crystals have dimensions of 6.3 mm transaxially, 6.3 mm axially and 30 mm radially. The crystals are arranged in detection units (blocks) consisting of 6×6 crystals, coupled to a single four-anode square photomultiplier. The 24 rings of the PET system allow 47 images (corresponding to 24 direct and 23 cross planes) to be obtained, spaced by 3.27 mm, and covering an axial field of view (FOV) of 15.7 cm. The PET tomograph can acquire data in both two-dimensional (2D) and three-dimensional (3D) configurations. In both 2D and 3D configurations, the energy window of the system is set to 375–650 keV, while the coincidence time window is set to 11.7 ns. The system is equipped with 0.8-mm-thick and 54-mm-long tungsten septa. The septa, which define the image planes in the 2D scanning configuration, can be automatically retracted from the scanner FOV, to allow the fully 3D acquisition modality. When the system is working in the 2D configuration, the axial combination is five and six planes for direct and cross planes

**Table 1.** Discovery ST: CT—main technical characteristics

| Scan mode | Helical, axial, scout |
|---|---|
| Aperture (cm) | 70 |
| Maximum scan field of view (cm) | 50 |
| No. of slices per rotation | 4–8 |
| Nominal slice width (mm) | 0.625, 1.25, 2.5,3.75, 5, 7.5, 10 |
| Tube voltage (kV) | 80, 100, 120, 140 |
| Tube current (mA) | 10–440 in 10-mA increments |
| Detector material | Solid state (Polycrystalline ceramic-Hi-lightLumex) |
| No. of elements along Z-axis | 16 |
| No. of detectors per row | 912 |
| Total effective length of detector array at isocentre (mm) | 20 |
| Variable scan speed (s) | 0.5–4 |
| Helical pitch | 3 HQ (high quality), 6 HS (high speed) |
| Max coverage (s/m) | 17 |
| Maximum continuous scan time (s) | 120 |
| Helical interpolation algorithms available | 180° LI, 360° and z-filter interpolation |
| Heat capacity (MHU) | 6.3 |
| Maximum power (kW) | 53.2 |

**Table 2.** Discovery ST: PET—main technical characteristics

| | |
|---|---|
| Detector ring diameter (cm) | 88.6 |
| Detector material | BGO |
| No. of individual crystals | 10,080 |
| No. of crystals/ring | 420 |
| No. of detector rings | 24 |
| No. of image planes | 47 |
| Crystal size ($mm^3$) | 6.3×6.3×30 |
| Face of crystal block ($mm^2$) | 38×38 |
| Crystal in a block | 6×6 |
| No. of detector blocks | 280 |
| No. of detector modules | 35 |
| Tungsten collimator size (mm) | 0.8 thick and 54 long |
| Patient port diameter (cm) | 70 |
| Axial field of view (cm) | 15.7 |
| Transaxial field of view (cm) | 70 |
| Axial sampling interval (mm) | 3.27 |
| Coincidence window width (ns) | 11.7 |
| Energy window (keV) | 375–650 |
| External pin source | $^{68}$Ge (55.5 MBq) |

respectively. In the 3D configuration, the oblique axial coincidence acceptance is up to ±23 planes.

The PET component has a pin radioactive source of $^{68}$Ge 55.5 MBq, which is used for the system calibration and for the daily quality test.

The main technical characteristics of the new PET/CT integrated system are summarised in Tables 1 and 2 for CT and PET, respectively.

Characterisation of the PET performance was accomplished by following the NEMA NU 2-1994 and NEMA NU 2-2001 standards, for both 2D and 3D acquisition configurations.

## NEMA NU 2-1994 (N-94) measurements

### *Spatial resolution*

*Source preparation and acquisition protocol.* A stainless steel needle [internal diameter (ID), 1 mm; outside diameter (OD), 1.5 mm; length, 16 cm] was used as the line source (LS). The LS was filled with approximately 18.5 MBq of $^{18}$F. By using a source holder attached to the bed of the scanner, the LS was suspended in air and positioned in the centre ($x$=0 cm, $y$=0 cm) of the transverse FOV.

Three 2D emission (EM) scans of 60 s each were acquired with the source at: (1) $x$=0 cm, $y$=1 cm, (2) $x$=0 cm, $y$=10 cm and (3) $x$=0 cm, $y$=20 cm. A second set of acquisitions was taken in 3D when the activity in the LS was approximately 5.55 MBq.

*Reconstruction and data analysis.* Data were corrected for dead-time losses, random coincidences, geometry and crystal normalisation. For each position of the LS, data were reconstructed as follows:

- 2D) Reconstruction algorithm: filtered back-projection (transaxial filter: ramp, cut-off: 4 mm); FOV: 6.4 cm; image matrix size: 256×256
- 3D) Reconstruction algorithm: 3D reprojection (transaxial filter: ramp, cut-off: 4 mm; axial filter: ramp, cut-off: 4 mm); FOV: 6.4 cm; image matrix size: 256×256.

Spatial resolution was measured as full-width at half-maximum (FWHM) and full-width at tenth-maximum (FWTM) of the line spread function by interpolation between adjacent pixels on the radial (vertical) and tangential (horizontal) profiles, respectively.

### *Scatter fraction*

*Source preparation and acquisition protocol.* A stainless steel needle (ID, 1 mm; OD, 1.5 mm; length, 20 cm) was also used for the scatter fraction (SF) measurements. The LS was filled with approximately 11.1 MBq of $^{18}$F with the aim of maintaining the dead-time losses at less than 5% and the random coincidences rate at less than 5% with respect to the total event rate of coincidences. The LS was positioned in a water-filled cylinder (diameter, 20 cm; length, 20 cm), which was centred, both in the transverse plane and along the z axis of the scanner FOV, by means of a source holder, attached to the scanner bed.

Three EM scans (15 min each) were acquired in 2D mode with the LS positioned in the phantom at: (1) $x$=0 cm, $y$=0 cm; (2) $x$=0 cm, $y$=4 cm and (3) $x$=0 cm, $y$=8 cm. When the activity of the LS was approximately 3.7 MBq, three 3D EM scans were recorded with the LS in the same positions as in the 2D scans.

*Reconstruction and data analysis.* Raw data sinograms were used to calculate the SF, in both 2D and 3D (after single slice rebinning). Data were corrected for random coincidences, dead-time losses, geometry and crystal normalisation. For the LS positioned off centre, the maximum of the LS profile in each projection angle was found and the profile shifted to be aligned with the central pixel. For all positions, the projection profiles were summed over angles to generate a single average projection profile. The scatter component within the peak of the profile was estimated by assuming a constant background, the level of which was determined by the average of the pixel intensities near the edge of the peak (±2 cm). The scatter component outside the peak was estimated over a fixed FOV of 24 cm diameter.

The SF was then calculated for each plane as:

$$SF = \frac{[R_s(0) + 8R_s(4) + 16R_s(8)]}{[R_{tot}(0) + 8R_{tot}(4) + 16R_{tot}(8)]} \quad (1)$$

where $R_s$ is the count rate of scattered events (at 0, 4 and 8 cm) and $R_{tot}$ is the total (trues + scatter) count rate.

### *Sensitivity*

*Source preparation and acquisition protocol.* A cylindrical phantom (diameter, 20 cm; length, 20 cm) uniformly filled with a solution of water and $^{18}$F was used to measure the sensitivity of the PET system for true events. An amount of 21.05 MBq of $^{18}$F was used to fill the phantom with the aim of maintaining the dead-time losses at less than 2% and the random coincidences rate at less than 2% with respect to the total event rate of coincidences. Using a source holder attached to the bed of the scanner, the phantom was centred both in the transverse plane and along the z axis of the scanner FOV.

An EM scan of 15 min was acquired in 2D mode. A second acquisition (15 min) was then performed in 3D mode, when the activity decayed at a level of 3.58 MBq.

*Reconstruction and data analysis.* Raw data sinograms (both 2D and 3D), corrected for random coincidences and dead-time losses,

were used in the analysis of sensitivity. Sensitivity ($S$) for true ($T$) events for each plane (direct and cross) was calculated as:

$$S = \frac{C_{TOT,120mm}}{T_{acq}} \left( \frac{1 - SF}{a_{ave}} \right) A \quad (2)$$

where $C_{TOT,120\ mm}$ is the total counts in each plane within a radius of 120 mm, $a_{ave}$ is the average activity in the phantom during the time of the measurement, $T_{acq}$ is the duration of the acquisition and SF is the scatter fraction for each plane.

The total system sensitivity was calculated by summing $S$ over all the planes of the PET system.

The sensitivity in 3D was calculated as for 2D, after single slice rebinning of the 3D data set.

### *Count rate losses and randoms*

*Source preparation and acquisition protocol.* A cylindrical phantom (diameter, 20 cm; length, 20 cm) uniformly filled with a solution of water and $^{18}$F was used for the count rate losses and randoms (CRL&R) test. The activity at the beginning of the experiment was 1,889.59 MBq for the 2D test, while 456.6 MBq was used for the 3D test. The phantom was positioned at $x$=0 cm and $y$=0 cm and axially centred in the scanner FOV.

A CT scan of the phantom was acquired to be used for attenuation correction (AC). The CT scan was performed at 140 kV and 90 mA. Eighteen 2D EM frames were acquired. Frames 1–4 were acquired for 900 s with no delay between consecutive frames. The remaining 14 frames were acquired for 1,500 s with a delay of 1,500 s between pair of consecutive frames. A delayed events (DE) circuit allowed an estimate of random coincidences during acquisition.

*Reconstruction and data analysis.* Raw data sinograms were used in the analysis of the CRL&R test. The total (trues + scatter + randoms) count rate and the DE random coincidences rate were measured over a transverse FOV of 24 cm, as a function of the radioactivity decay. The $T$ rate ($R_{trues}$) was determined by subtracting the randoms and scatter rates ($R_{random}$, $R_{scatter}$) from the total event rate. The noise equivalent count (NEC) rate was then calculated as:

$$NEC = \frac{R_{trues}^2}{R_{trues} + R_{scatter} + kR_{randoms}} \quad (3)$$

The total, $T$, random, scatter and NEC rates were plotted against the activity concentration in the phantom. An NEC rate curve was generated with $k$=2, as $R_{random}$ was estimated by the DE technique [NEC($k$=2)].

The percentage of the dead-time (%DT) as a function of the activity concentration in the phantom was calculated as:

$$\%DT = 100 \left( 1 - \frac{T}{T_{extrap}} \right) \quad (4)$$

where $T_{extrap}$ is the linear function of the $T$ events rate, extrapolated from the low count rate data.

### *Count rate correction accuracy*

*Source preparation and acquisition protocol.* Data acquired for the CRL&R test were also used for the evaluation of the count rate correction accuracy.

*Reconstruction and data analysis.* Data were corrected for random coincidences, geometry, normalisation, dead-time losses, scatter and attenuation. Data were reconstructed as follows:

- 2D) Reconstruction algorithm filtered back-projection (transaxial filter: ramp, cut-off: 4 mm); FOV, 25.5 cm; image matrix size, 128×128.
- 3D) Reconstruction algorithm 3D reprojection (transaxial filter: ramp, cut-off: 4 mm; axial filter: ramp, cut-off: 4 mm); FOV, 25.5 cm; image matrix size, 128×128.

Once reconstructed, the images were analysed by drawing a region of interest (ROI) with a diameter of 18 cm centred on the phantom image. The resulting dead-time corrected $T$ count rate ($R$) was plotted against the activity concentration in the phantom and the percentage residual dead-time error $\%\Delta r$ was calculated as:

$$\%\Delta r = 100 \left( 1 - \frac{R}{R_{extrap}} \right) \quad (5)$$

where $R_{extrap}$ is the linear function of $R$, extrapolated from the low count rate data (using the last three frames). Residual errors ($\%\Delta r$) were calculated for each slice as a function of the activity concentration.

### *Scatter correction accuracy*

*Source preparation and acquisition protocol.* The accuracy of the scatter correction was assessed using a cylindrical phantom (diameter, 20 cm; length, 20 cm) uniformly filled with a solution of water and $^{18}$F. Approximately 74 MBq of $^{18}$F was used to fill the phantom. To create a region with no activity, where the accuracy of the scatter correction could be evaluated, a cylinder (5 cm diameter, same length as the phantom), filled with "cold" non-radioactive water, was placed inside the phantom. The phantom was attached to the patient table using an adjustable mounting bracket, positioned at $x$=0 cm, $y$=–2.5 cm and axially centred.

A CT scan of the phantom was acquired to be used for AC (140 kV, 90 mA). An EM 2D scan was acquired for 30 min. A second EM 3D scan was then acquired when the activity decayed at the level of approximately 18.5 MBq, for the same acquisition time.

*Reconstruction and data analysis.* Data (both 2D and 3D) were reconstructed using algorithms and parameters as described in the "Count rate correction accuracy" section with the exception of the image matrix size, which, in this case, was 256×256.

Data analysis was performed on the reconstructed images by drawing, on each slice, 12 circular ROIs (3 cm diameter). One ROI was drawn on the non-radioactive cold insert, while the others were drawn on the hot radioactive background.

For each slice the accuracy of the scatter correction, as residual error $\Delta SF_{corr}$ was then calculated as:

$$\Delta SF_{corr} = 100 \left( \frac{C_{cold\_insert}}{C_{avg}} \right) \quad (6)$$

where $C_{cold\_insert}$ is the number of counts in the cold_insert ROI and $C_{avg}$ is the average number of counts in the other 11 ROIs.

### *Attenuation correction accuracy*

*Source preparation and acquisition protocol.* The accuracy of attenuation correction (AC) was assessed using a cylindrical phan-

tom (diameter, 20 cm; length, 20 cm) uniformly filled with a solution of water and $^{18}$F. Approximately 74 MBq of $^{18}$F was used to fill the phantom. To create regions where the accuracy of AC could be evaluated, three cylinders with a diameter of 5 cm were placed inside the phantom. The first cylinder was empty (filled with air), the second was filled with non-radioactive water and the third was of Teflon.

The phantom was attached to the patient table using an adjustable mounting bracket and then positioned at $x$=0 cm, $y$=−2.5 cm and axially centred.

A CT scan of the phantom was acquired to be used for AC (140 kV, 90 mA). An EM 2D scan was acquired for 30 min. A second EM 3D scan was then acquired when the activity decayed at the level of 18.5 MBq, for the same acquisition time.

*Reconstruction and data analysis.* Both 2D and 3D data were reconstructed using the algorithms and the parameters as described in the "Count rate correction accuracy" section with the exception of the image matrix size, which, in this case, was 256×256.

Data analysis was performed on the reconstructed images by drawing on each slice 12 circular ROIs of 3 cm in diameter. Three ROIs were drawn on each of the "cold" non-radioactive inserts (air, water and Teflon), while the other nine ROIs were drawn on the hot radioactive background. The average counts in the hot background $C_N$ were calculated over the nine ROIs. For each slice, the accuracy of AC was then calculated for each insert as residual attenuation error $\Delta AC_{insert}$:

$$\Delta AC_{insert} = 100\left(\frac{C_{insert}}{C_N}\right) \quad (7)$$

where $C_{\text{insert}}$ is the number of counts in the ROI for each insert (air, water or Teflon).

## NEMA NU 2-2001 (N-01) measurements

### *Spatial resolution*

*Source preparation and acquisition protocol.* A solution of water and $^{18}$F with a concentration higher than 185 MBq/cc was prepared. A drop of the solution was then used to produce three point sources (PS). Glass capillaries with an ID of 1 mm were used to contain the PS. Using a source holder, the three glass capillaries containing the PS were positioned in the scanner FOV at: (1) $x$=0 cm, $y$=1 cm; (2) $x$=0 cm, $y$=10 cm; (3) $x$=10 cm, $y$=0 cm. Once in place, the three point sources where aligned (axially) in the scanner FOV using laser lights.

Two sets of EM measurements, consisting of 20 acquisitions axially spaced at 0.5 mm were performed in 2D. The two sets of measurements were centred at two axial positions in the scanner FOV: in the centre and at one-quarter of the axial FOV (3.8 cm). Acquisition time for each single acquisition was 1 min. The two sets of measurements were then repeated in 3D mode.

*Reconstruction and data analysis.* Image reconstruction of the PS was performed for both 2D and 3D data as for the spatial resolution N-94 test, with the exception of the extension of the FOV, which in this case was 25.0 cm, so that each of the three sources could be visualised.

Transverse spatial resolution was calculated for each PS position as FWHM and FWTM of the resulting point spread function, by interpolation between adjacent pixels on the radial (vertical) and tangential (horizontal) profiles. An axial profile was derived from the number of counts in each slice against the slice number and axial resolution was measured as the FWHM and FWTM of such a profile. Radial and tangential resolutions (FWHM and FWTM) for each radial position (1 and 10 cm) were averaged over both axial positions.

### *Sensitivity*

*Source preparation and acquisition protocol.* A solution of water and $^{18}$F with a concentration greater than 1.7 MBq/cc was prepared. The LS was prepared by filling a polyethylene tube (ID 1 mm, OD 3 mm) in the central 70 cm and activity was measured. The N-01 sensitivity phantom consists of five concentric aluminium tubes, 700 mm long and stacked one inside the other. The diameters of each tube are:

- 1st tube: ID 3.9 mm, OD 6.4 mm
- 2nd tube: ID 7.0 mm, OD 9.5 mm
- 3rd tube: ID 10.2 mm, OD 12.7 mm
- 4th tube: ID 13.4 mm, OD 15.9 mm
- 5th tube: ID 16.6 mm, OD 19.1 mm

Using a phantom holder, the LS, inserted in the smallest aluminium tube, was centred along the x, y and z axes of the scanner FOV.

A set of five 2D EM scans was acquired. In each subsequent scan (60 s each), an additional aluminium tube was added around the LS, so that during the last scan, the LS was surrounded by the five aluminium tubes. A second set of measurements (five scans) was taken to estimate the sensitivity in 3D mode. The phantom was then positioned at $x$=10 cm and $y$=0 cm with respect to the centre of the scanner FOV and 2D and 3D measurements were carried out following the same protocol as before (for $x$=0 and $y$=0).

*Reconstruction and data analysis.* Raw data sinograms were used in the analysis of sensitivity. The five scans in each set of measurements were corrected for radioactive decay. The analysis was first performed for each plane. Count rates $R_j$ ($j$=1, 5) were plotted versus the sleeve thickness $X_j$. The count rate in the absence of attenuation ($R_0$) was calculated by extrapolating the resulting exponential attenuation curve to $X_j$=0.

$$R_j = R_0 \exp(-2\mu X_j) \quad (8)$$

where μ is the linear attenuation coefficient.

The sensitivity for each plane was calculated by dividing the extrapolated $R_0$ by the measured activity. Total system sensitivity was calculated as the sum of sensitivity per plane over the 47 planes.

### *Scatter fraction and count rates*

*Source preparation and acquisition protocol.* The phantom used for the measurement consists in a 20-cm-diameter solid polyethylene cylinder with an overall length of 70 cm. The phantom has a hole at 4.5 cm from its centre, which goes through the whole phantom, parallel to its central axis. In the hole a Teflon LS (ID 2.3 mm), as long as the phantom, can be inserted to contain radioactivity. The LS was filled in its 70-cm central part with a solution of water and $^{18}$F. Two tests were performed, in 2D and 3D, with an initial activity of 2,664 MBq and 1,776 MBq, respectively. In both tests, the phantom was positioned at $x$=0 cm, $y$=0 cm and axially

centred in the scanner FOV. In both acquisitions, random coincidences were measured by the DE technique.

In each test (2D and 3D), 22 EM frames were acquired. Frames 1–4 were acquired for 900 s with no delay between consecutive frames. The remaining 18 frames were acquired for 1,500 s with a delay of 1,500 s between each consecutive pair of frames.

*Reconstruction and data analysis.* Raw data sinograms were used in the analysis of the scatter fraction and count rates (SF&CR) test. 3D sinograms were rebinned by using a single slice-rebinning algorithm.

Scatter component was calculated as for the N-94 over a fixed FOV of 40 cm diameter. Only the final frames of the SF&CR test (when the randoms rate was negligible, below 1%) were used to calculate the scatter fraction. Scatter fraction was calculated as the ratio between scatter component and total events.

The total counts rate within a 24-cm transverse FOV was determined as a function of the radioactivity decay. The $T$ rate ($R_{trues}$) was determined by subtracting the randoms and scatter rates from the total prompts event rate ($R_{total}$). The NEC rate was calculated as in Eq. 3. Two NEC rate curves were then generated, with $k$=1 and $k$=2.

### *Accuracy of corrections for count losses and randoms*

*Source preparation and acquisition protocol.* The same data set as was acquired for the SF&CR test was used.

*Reconstruction and data analysis.* Data were reconstructed with all count rate-dependent corrections (dead-time losses and random coincidences) applied. A circular ROI (18 cm diameter) was drawn, centred on the reconstructed images of the phantom.

2D and 3D data sets were reconstructed as for the count rate accuracy test of the N-94. The resulting dead-time and random-corrected trues image count rate ($R$) was plotted as a function of activity concentration.

The residual dead-time error $\%\Delta r$ was then calculated as:

$$\%\Delta r = 100\left(1 - \frac{R}{R_{extrap}}\right) \tag{9}$$

where $R_{extrap}$ is the linear function of the true count rate extrapolated from the low count rate (where dead-time and random coincidences rate are negligible).

### *Image quality—attenuation and scatter correction accuracy*

*Source preparation and acquisition protocol.* Overall image quality (IQ), as well as attenuation and scatter correction accuracy, was evaluated using a phantom simulating a human torso in size and shape. The IQ phantom contains six co-axial isocentre spheres with diameters of 1.0, 1.3, 1.7, 2.2, 2.8 and 3.7 cm. A cylindrical insert of 5 cm diameter, as long as the phantom, is also positioned in the centre of the phantom. The cylinder is a cold insert with a density of 0.30 g/cc to simulate the lungs. Four of the spheres, with diameters of 1.0, 1.3, 1.7 and 2.2 cm, are used to simulate hot lesions, while the other two are used to simulate cold lesions. The phantom was filled with a solution of water and $^{18}$F (5.3 kBq/cc), and the spheres with a concentration eight times higher than the background, to simulate a lesion to background (L/B) ratio of 8. In a second experiment, radioactivity concentration in the hot spheres was such that L/B was 4. Once filled, the phantom was positioned with the spheres both in the transverse plane and along the z axis of the scanner FOV. To simulate body activity from outside of the scanner FOV, the phantom used for the SF&CR test was positioned at one edge of the IQ phantom. For this test, the LS of the external phantom was filled with an activity of 165.5 MBq.

A CT scan of the phantom was acquired to be used for AC (140 kV, 90 mA). For both the experiments (L/B=8 and 4), six interleaved acquisitions (2D and 3D) were performed. The acquisition time for each 2D and 3D measurement was 8 min and 20 s and 7 min and 19 s respectively. These times were derived, based on a whole-body examination designed to cover a 100-cm axial FOV in 60 min, using a slice overlap for 2D and 3D mode of 5 and 11 slices, respectively.

*Reconstruction and data analysis.* Data were corrected for random coincidences, geometry, normalisation, dead-time losses, scatter and attenuation.

Image reconstruction of the IQ phantom data was performed as follows:

- 2D) Reconstruction algorithm ordered subsets-expectation maximisation (OSEM) (number of subsets, 21; number of iterations, 2; loop filter, 3.91 mm FWHM; post-filter, 5.45 mm FWHM); FOV, 50 cm; image matrix size, 128×128.
- 3D) Reconstruction algorithm FORE-Iterative (weighted least square; number of subsets, 32; number of iterations, 3; loop filter, 3.91 mm FWHM; post-filter, 4.29 mm FWHM); FOV, 50 cm; image matrix size, 128×128.

In order to evaluate the hot and cold sphere contrast, circular ROIs with a diameter equal to the physical size of each sphere were drawn on CT images and copied to PET images. Twelve background ROIs (37 mm diameter) were drawn on the central slice and on slices ±10 mm and ±20 mm from the central slice. ROIs of smaller size (10, 13, 17, 22, 28 mm) were drawn concentric to the 37-mm background ROIs. Finally, an ROI of 5 cm in diameter was drawn (in each slice of the phantom) on the central cylindrical insert to assess the accuracy of the attenuation and the scatter correction.

Different parameters used to evaluate the IQ test were:

a) The hot sphere contrast recovery coefficient ($HC\_RC$) calculated as:

$$HC\_RC = \frac{\left(C_{hot}/C_{bkgd} - 1\right)}{\left(a_{hot}/a_{bkgd} - 1\right)} \tag{10}$$

where $C_{hot}$ and $C_{bkgd}$ are the average of the counts measured in the hot spheres ROI and the average counts in all background ROIs respectively, while $a_{hot}/a_{bkgd}$ is the ratio of the activities in the hot sphere and background (this ratio is nominally 8 or 4, but the actual values as measured by a well counter were used in the calculations).

b) The cold sphere contrast ($CC$) calculated as:

$$CC = 1 - \left(C_{cold}/C_{bkgd}\right) \tag{11}$$

where $C_{cold}$ is the average of the counts measured in the cold spheres ROI.

c) The accuracy of attenuation and scatter correction, calculated as the residual error in the lung region as:

$$\Delta AC_{lung} = 100\left(C_{lung}/C_{bkgd}\right) \tag{12}$$

where $C_{lung}$ is the average counts in the lung insert ROI.

d) The background variability, calculated as:

$$BV_j = 100\left(SD_j / C_{bkgd,j}\right) \quad (13)$$

where $SD_j$ is the standard deviation of the background ROI counts for sphere $j$.

## Results

*NEMA NU 2-1994 measurements*

Spatial resolution

The average values of the transverse spatial resolution (FWHM and FWTM) for radial and tangential profiles are shown in Table 3 for both 2D and 3D configurations. The values for all the positions of the LS and for direct, cross and all acquisition planes are presented. In both 2D and 3D, direct and cross plane spatial resolution values are very similar. As expected, in view of the circular geometry of the scanner, in 2D radial resolution is worse than tangential resolution. This is not true for the FWTM in 3D owing to the weight on the mean of the values for external planes, as shown in Fig. 1. In general, spatial resolution in 2D is slightly better than in 3D.

Scatter fraction

The values of the scatter fraction (minimum, maximum and average) for direct, cross and all planes in 2D and 3D mode are reported in Table 3. In 2D, as expected, the cross planes have a slightly higher scatter fraction with respect to the direct planes owing to the wider acceptance angle (five adjacent planes are used to generate a direct plane, and six adjacent planes are used to generate a cross plane), while, in 3D, the scatter fraction is more uniform throughout all the slices of the system.

Sensitivity

In Fig. 2 the slice sensitivity profiles for *T* events are shown for 2D and 3D configuration, respectively. Table 3 reports PET *T* sensitivity values for direct, cross and all planes, in 2D and 3D. The reported sensitivity values for direct and cross planes were averaged over planes 5–43 and 6–42, respectively, excluding the most external planes because of the lower number of planes contributing to their generation.

The total system sensitivity for *T* events was 8,567 cps/kBq/cc and 36,649 cps/kBq/cc in 2D and 3D,

**Table 3.** NEMA NU 2-1994: performance characteristics

| | | | | 2D | | | 3D | | |
|---|---|---|---|---|---|---|---|---|---|
| | | | | Direct | Cross | All | Direct | Cross | All |
| Spatial resolution (mm) | 1 cm | FWHM | R | 6.61 | 6.59 | 6.60 | 6.73 | 6.71 | 6.72 |
| | | | T | 5.95 | 5.98 | 5.96 | 6.65 | 6.63 | 6.64 |
| | | FWTM | R | 12.55 | 12.58 | 12.56 | 13.27 | 13.23 | 13.25 |
| | | | T | 11.35 | 11.39 | 11.37 | 13.33 | 13.30 | 13.31 |
| | 10 cm | FWHM | R | 7.51 | 7.52 | 7.51 | 7.92 | 7.93 | 7.92 |
| | | | T | 6.67 | 6.66 | 6.67 | 7.55 | 7.50 | 7.53 |
| | | FWTM | R | 13.34 | 13.41 | 13.38 | 14.31 | 14.33 | 14.32 |
| | | | T | 12.65 | 12.63 | 12.64 | 15.15 | 14.89 | 15.02 |
| | 20 cm | FWHM | R | 8.03 | 8.06 | 8.04 | 8.36 | 8.36 | 8.36 |
| | | | T | 6.85 | 6.88 | 6.87 | 7.92 | 7.88 | 7.90 |
| | | FWTM | R | 15.18 | 15.15 | 15.16 | 15.01 | 15.02 | 15.01 |
| | | | T | 12.70 | 12.74 | 12.72 | 15.97 | 15.68 | 15.83 |
| Scatter fraction (%) | Minimum | | | 14.14 | 14.62 | 14.14 | 28.76 | 28.26 | 28.26 |
| | Maximum | | | 15.80 | 16.30 | 16.30 | 30.79 | 30.92 | 30.93 |
| | Average over planes | | | 14.99 | 15.62 | 15.31 | 30.02 | 30.21 | 30.13 |
| True events sensitivity (cps/kBq/cc) | Minimum | | | 184.51 | 206.94 | 37.77 | 308.60 | 369.84 | 45.91 |
| | Maximum | | | 191.38 | 213.58 | 213.58 | 1493.03 | 1525.42 | 1525.42 |
| | Average over planes | | | 187.22 | 211.26 | 182.31 | 890.24 | 928.58 | 780.00 |
| Scatter correction accuracy (%) | Minimum | | | –3.20 | –3.38 | –3.38 | –9.59 | –11.67 | –11.67 |
| | Maximum | | | 6.33 | 4.91 | 6.33 | –4.28 | –3.91 | –3.91 |
| | Average over planes | | | 1.59 | 1.70 | 1.64 | –7.29 | –7.36 | –7.32 |
| Attenuation correction accuracy (%) | Average—water | | | 2.86 | 3.25 | 3.05 | –2.64 | –3.62 | –3.12 |
| | Average—air | | | 7.12 | 6.89 | 7.01 | 12.43 | 12.20 | 12.32 |
| | Average—solid | | | –30.86 | –29.70 | –30.29 | –46.16 | –47.19 | –46.66 |

Spatial resolution: R, radial; T, tangential. Sensitivity values for direct and cross planes were averaged over planes 5–43 and 6–42, respectively

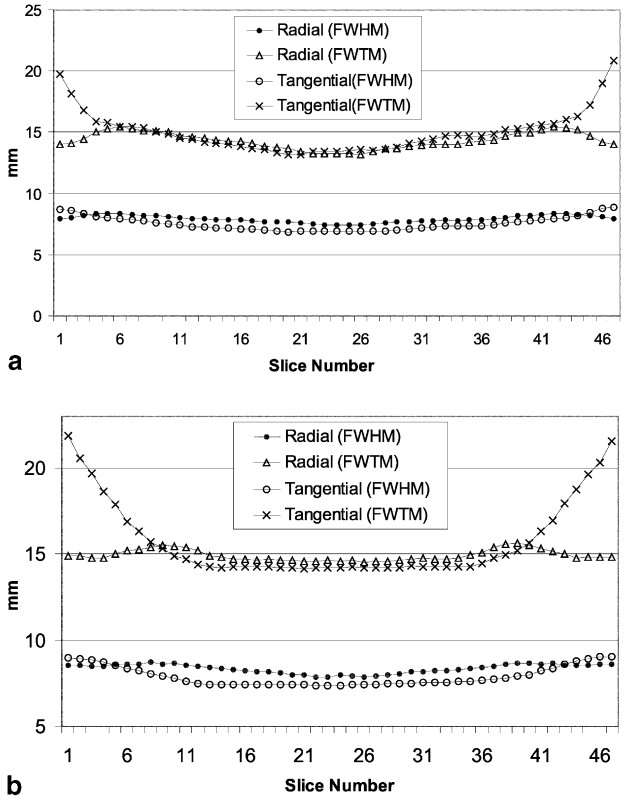


**Fig. 1a, b.** N-94: 3D spatial resolution (transverse) vs plane number: **a** LS positioned at 10 cm off axis, **b** LS positioned at 20 cm off axis

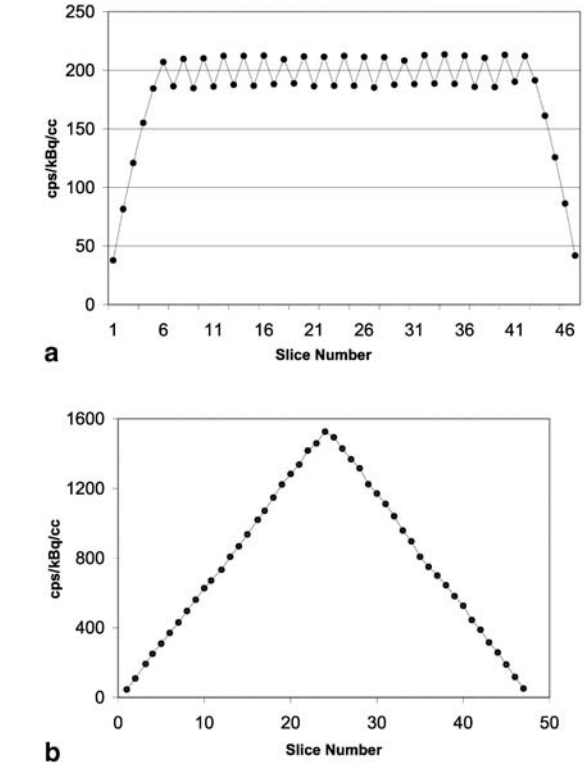


**Fig. 2a, b.** N-94: sensitivity for true events (slice sensitivity profile). **a** 2D, **b** 3D

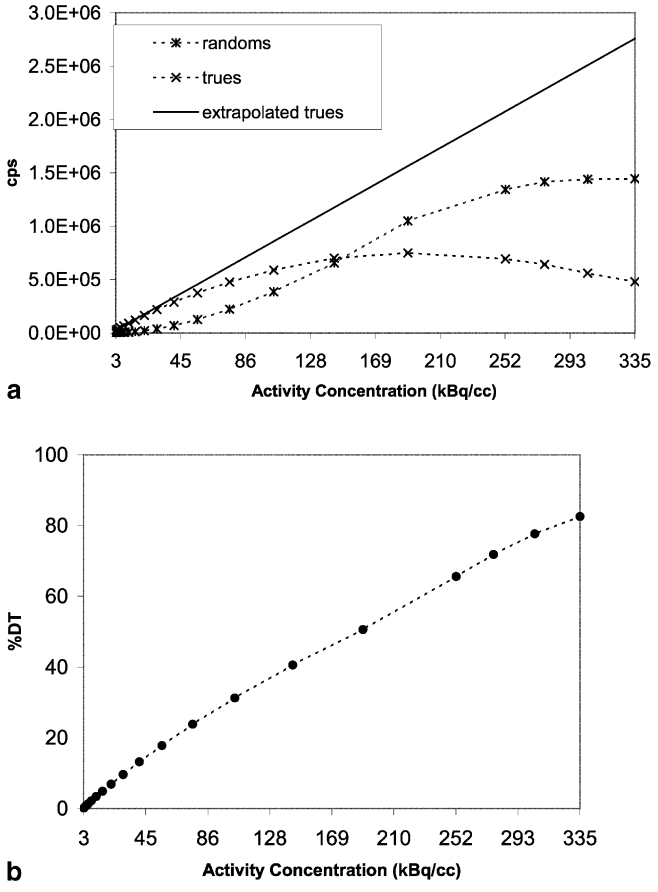


**Fig. 3a, b.** N-94: 2D count rate losses and random test: **a** count rate vs activity concentration, **b** percentage of the system dead time (*%DT*) vs activity concentration

respectively, and thus approximately 4.3 times higher in 3D than in 2D.

## Count rate losses and randoms

Figure 3 shows the response of the D-ST PET system in terms of count rate (Fig. 3a) and %DT (Fig. 3b) as a function of the activity concentration. Figure 4 shows the corresponding response of the system (Fig. 4a for the count rate, Fig. 4b for the dead time) in 3D. A slight discontinuity in the %DT curve can be observed in 2D at about 190 kBq/cc and in 3D at about 44.4 kBq/cc. This discontinuity can also be observed in the *T*, random and NEC rate curves, which, at those values of radioactivity concentration, bend towards a lower count rate (smoothly in 2D and sharply in 3D). This effect is explained by the processing capability of the events sorter board, which handles up to about 10 million events per second. When this events rate is exceeded, events are discarded and not recorded. It is to be noted that, in both FDG brain and whole-body studies, radioactivity in the FOV is low with respect to this critical situation. In fact, clini-

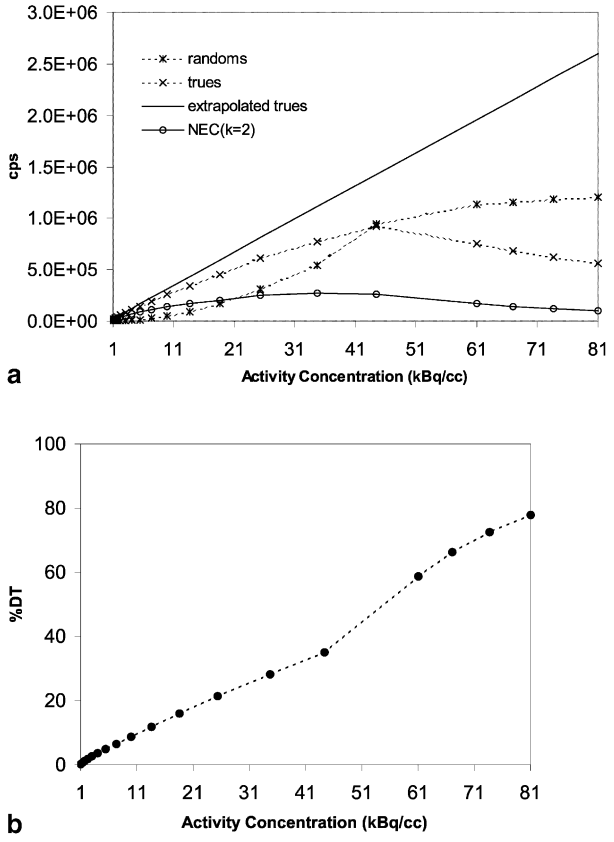


**Fig. 4a, b.** N-94: 3D count rate losses and random test: **a** count rate vs activity concentration, **b** percentage of the system dead time (*%DT*) vs activity concentration

**Table 4.** NEMA NU 2-1994: 2D and 3D count rate losses and randoms test

| | 2D | | 3D | |
|---|---|---|---|---|
| | kBq/cc | kcps | kBq/cc | kcps |
| Peak trues | 189.81 | 750 | 44.03 | 922 |
| 50% dead-time | 186.48 | 744 | 53.28 | 834 |
| Trues = randoms | 150.59 | 686 | 44.03 | 921 |

cal count rates are less than 1 million counts for prompt events.

In Table 4 figures of merit representative for the count rate and randoms tests are reported as the values of the activity concentration (kBq/cc) and of the *T* events rate (kcps) at which the following conditions are verified: (a) peak of *T* events rate, (b) 50% of the system dead-time, (c) trues rate = randoms rate. All conditions are verified in 2D at a higher activity concentration and at a slightly lower count rate than in 3D.

### Count rate correction accuracy

The minimum and the maximum dead-time residual errors $\%\Delta r$ estimated over all slices for the activity concentration at 50% of the system dead-time were –0.88% and 11.31% in the 2D configuration and –12.5% and –6.4% in the 3D configuration, respectively.

### Scatter correction accuracy

In Table 3 the results obtained for the scatter correction accuracy test, for both the 2D and the 3D configuration, are shown. The minimum and maximum error and the average error over planes are reported. While in 2D the average residual error after scatter correction is less than 2% (in the range –4 to +6), in 3D the residual error after scatter correction is of the order of –7% (in the range –12 to –4). The negative value of the residual error indicates a scatter overestimation during correction.

### Attenuation correction accuracy

In Table 3 the results obtained for the attenuation correction accuracy test are shown for both the 2D and the 3D acquisition configuration. The error for the water and air inserts is relatively small, while the error for the solid material (Teflon) is big. This is because Teflon was assumed to be bone material during the process of conversion of its CT number into attenuation coefficient for 511 keV. Teflon in fact has a high CT number [15], which is converted to attenuation coefficient for 511 keV assuming it as bone material. The linear attenuation coefficient for Teflon at 511 keV is 0.19 $cm^{-1}$, while the corresponding linear attenuation coefficient resulting from the conversion of the CT number was 0.14 $cm^{-1}$, with an error of –25%. This underestimation of the Teflon attenuation coefficient at 511 keV yields low (negative) activity values after attenuation (and scatter) correction. It should be noted that Teflon insert is not a suitable bone substitute for use in a CT scanner, and the use of a more appropriate bone-equivalent material should be considered for this test, in the case of PET/CT scanners.

## *NEMA NU 2-2001 Measurements*

### Spatial resolution

Transverse spatial resolution values in 2D and 3D are reported in Table 5. For the PS at ($x$=0 cm, $y$=1 cm), radial and tangential resolution values were averaged. Also, spatial resolution values for the PS at ($x$=0 cm, $y$=10 cm) and ($x$=10 cm, y=0 cm) were averaged.

Axial resolution values are also presented in Table 5. Spatial resolution is nearly isotropic, in particular in 3D at a radial distance of 10 cm from the centre of the FOV.

**Table 5.** NEMA NU 2-2001: performance characteristics

| | | | | 2D | | 3D | |
|---|---|---|---|---|---|---|---|
| Spatial resolution (mm) | 1 cm | FWHM | Radial and tangential average | 6.28 | | 6.29 | |
| | | FWTM | | 11.55 | | 11.49 | |
| | 10 cm | FWHM | Radial | 6.94 | | 7.01 | |
| | | | Tangential | 6.82 | | 6.64 | |
| | | FWTM | Radial | 12.38 | | 12.68 | |
| | | | Tangential | 13.12 | | 11.94 | |
| Axial resolution (mm) | 1 cm | FWHM | | 4.56 | | 5.68 | |
| | | FWTM | | 9.33 | | 11.94 | |
| | 10 cm | FWHM | | 6.11 | | 6.05 | |
| | | FWTM | | 12.35 | | 11.52 | |
| Sensitivity (cps/kBq) | 0 cm | | | 1.92 | | 8.99 | |
| | 10 cm | | | 1.95 | | 9.26 | |
| Scatter fraction (%) | | | | 19 | | 45 | |
| | | | | kcps | kBq/cc | kcps | kBq/cc |
| Count rate parameters | Peak trues rate | | | 270.99 | 113.64 | 292.15 | 20.38 |
| | Peak random rate | | | 728.32 | 113.64 | 1443.41 | 63.33 |
| | Peak scatter rate | | | 63.61 | 113.64 | 220.18 | 20.38 |
| | Peak NEC($k$=1) rate | | | 80.78 | 64.43 | 66.17 | 14.86 |
| | Peak NEC($k$=2) rate | | | 54.01 | 46.99 | 45.50 | 10.84 |

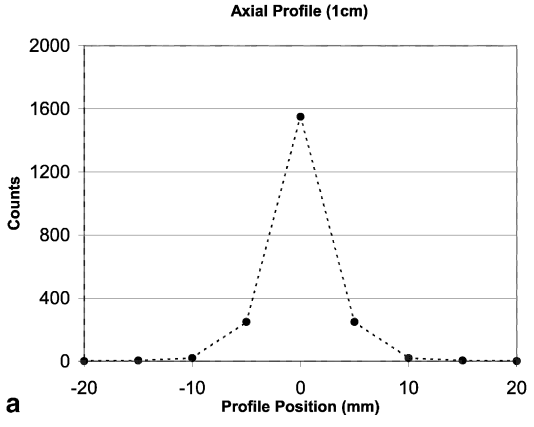


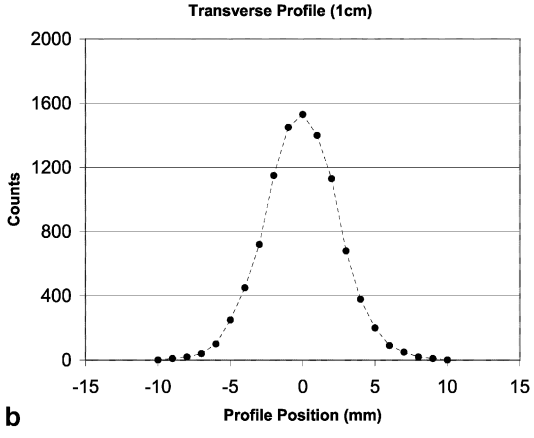


◀ **Fig. 5a, b.** N-01: 2D spatial resolution for a point source at 1 cm off centre: **a** axial profile, **b** transverse profile

In Fig. 5, the axial and transverse profiles for the 1 cm off-centre source are shown, as a representative example of the spatial response of the PET system.

## Sensitivity

The results of the sensitivity test for both 2D and 3D acquisition configurations are shown in Table 5. The system has very good sensitivity in both 2D and 3D. Sensitivity in 3D is approximately 4.3 times higher than in 2D.

Figure 6 shows the slice sensitivity profiles for $T$ events in 2D and 3D mode, respectively.

## Scatter fraction and count rate

Figures 7 and 8 show the results for the SF&CR tests in 2D and 3D.

Table 5 reports the values of scatter fraction in 2D and 3D, as well as the count rate of the system and the corresponding activity concentration at the peak $T$ rate, peak randoms rate, peak scatter rate, and peak NEC($k$=1) and NEC($k$=2) rates. The NEC($k$=1) peak is achieved

**Table 6.** NEMA NU 2-2001: IQ phantom—figures of merit

| | 2D Sphere diameter (cm) | | | | | | | 3D Sphere diameter (cm) | | | | | | |
|---|---|---|---|---|---|---|---|---|---|---|---|---|---|---|
| | 10 | 13 | 17 | 22 | 28 | 37 | | 10 | 13 | 17 | 22 | 28 | 37 | |
| *L/B=4* | | | | | | | | | | | | | | |
| Hot sphere recovery coeff. (%) | 24 | 37.3 | 57.3 | 68.7 | – | – | – | 20 | 37.6 | 52.3 | 69 | – | – | – |
| Cold sphere contrast (%) | – | – | – | – | 58 | 66.5 | – | – | – | – | – | 83 | 85 | – |
| Background variability (%) | 8 | 7 | 6 | 5 | 4 | 3 | – | 7 | 6 | 5 | 4 | 3 | 3. | – |
| Average residual (%) over "lung" insert | – | – | – | – | – | – | 23 | – | – | – | – | – | – | 16 |
| *L/B=8* | | | | | | | | | | | | | | |
| Hot sphere contrast (%) | 26.7 | 36 | 65 | 72 | – | – | – | 23.7 | 36.3 | 54.7 | 69.5 | – | – | – |
| Cold sphere contrast (%) | – | – | – | – | 60 | 70 | – | – | – | – | – | 80 | 82 | - |
| Background variability (%) | 10 | 9 | 8 | 6 | 5 | 4 | – | 9 | 8 | 7 | 5 | 5 | 4 | – |
| Average residual (%) over "lung" insert | – | – | – | – | – | – | 24 | – | – | – | – | – | – | 17 |

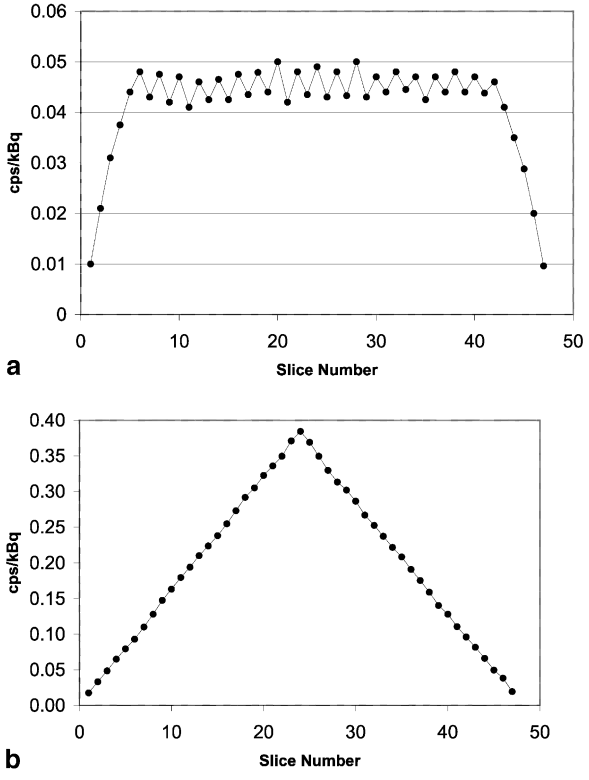


**Fig. 6a, b.** N-01: sensitivity for true events (slice sensitivity profile): **a** 2D, **b** 3D

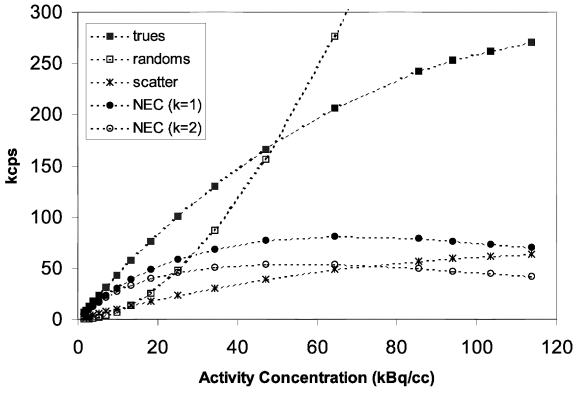


**Fig. 7.** N-01: 2D scatter fraction and count rate test. Trues, scatter, random, NEC($k$=1) and NEC($k$=2) rate vs activity concentration

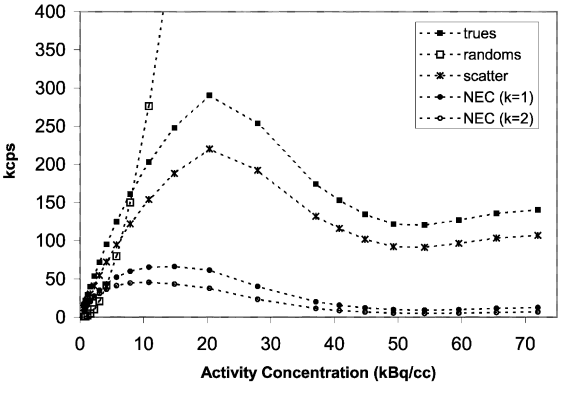


**Fig. 8.** N-01: 3D scatter fraction and count rate test. Trues, scatter, random, NEC($k$=1) and NEC($k$=2) rate vs activity concentration

with 66.17 kcps at 14.86 kBq/cc, while the NEC($k$=2) peak is achieved with 45.5 kcps at 10.84 kBq/cc.

Accuracy of corrections for count losses and randoms

The maximum error found for the 2D acquisition mode was 6.9% for activity concentrations below 64.43 kBq/cc [corresponding to the peak NEC($k$=1) rate]. In 3D, the maximum error was 1.9% for activity concentrations below 14.86 kBq/cc [corresponding to the peak NEC($k$=1) rate].

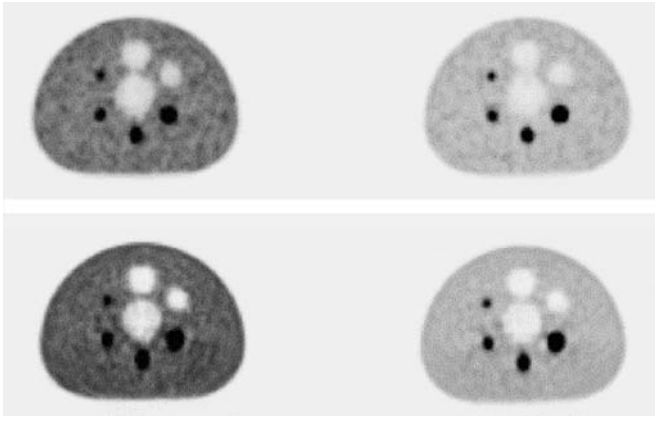

**Fig. 9.** Reconstructed image of the IQ phantom. *Top*, 2D image; *bottom*, 3D image; *left*, L/B=4 experiment; *right*, L/B=8 experiment

Image quality—attenuation and scatter correction accuracy

In Table 6 the results obtained for the IQ test are shown in terms of hot sphere recovery coefficient, cold sphere contrast, average residual attenuation and scatter correction error in the lung region and background variability. Hot sphere recovery coefficients are almost comparable in 2D and 3D for the L/B=4 experiment and slightly better in 2D than in 3D for the L/B=8 experiment. Cold sphere contrast is higher in 3D than in 2D. Attenuation and scatter correction residual error in the lung region, as well as background variability, are lower in 3D than in 2D.

In Fig. 9, a representative image of the IQ phantom is shown in the 2D and 3D studies, for the two L/B experiments. Qualitative analysis of the images confirms the quantitative results, previously described.

## Discussion

The new integrated PET/CT system Discovery ST (D-ST) has recently been installed in our institution. The D-ST was specifically designed for PET imaging in oncology, both for diagnostic applications and for applications in radiotherapy, to improve the definition of the radiation treatment plan based on the fused CT and PET images. The D-ST combines a state of the art multi-slice helical CT scanner and a state of the art PET tomograph, based on BGO detectors, and operating in both the 2D and the 3D acquisition modality. The PET scanner port has been enlarged to allow the positioning of radiotherapy patients, an option for a flat couch is available, and the architecture of the detection system is designed in order to yield high detection efficiency and isotropic resolution, to improve lesion detectability and lesion volume estimation.

The aim of this work was the physical characterisation of the PET performance of the D-ST according to the NEMA standard protocols. Both the N-94 and N-01 standards were considered. In the N-94 standard, the size of the phantoms (20 cm in diameter and 20 cm long) and the activity distributions in the phantoms (in most situations uniform) make the N-94 tests particularly suitable to assess the performance of the PET scanners in conditions comparable to those of neurological studies (distributed source). In this respect, several considerations need to be mentioned. The limited axial size of the N-94 phantoms (20 cm) does not allow the contribution of activity from outside the FOV to be taken into account (unless other non-standard objects are positioned adjacent to the phantom). This condition is unsuitable for the simulation of brain studies in patients, and also inappropriate for the simulation of whole-body studies. Furthermore, the N-94 standard was originally defined for tests performed in the 2D acquisition configuration. However, PET brain studies are currently usually performed in the 3D mode, in order to take advantage of the increased detection efficiency. Although the extension of the 2D N-94 tests to the 3D case could be methodologically straightforward, technically it is currently hampered in most commercial systems by the lack of the necessary software and analysis tools. The N-01 standard has been defined to account for the clinical evolution of PET into oncological diagnosis. The N-01 tests have thus been redesigned to simulate oncological FDG whole-body studies. In particular, N-01 uses 70-cm-long phantoms to account for the activity contribution from outside the FOV. In view of the potential of the 3D acquisition modality and its increasing clinical diffusion, N-01 tests are defined for both 2D and 3D acquisition configurations.

In this work, the physical characterisation of the D-ST was performed following both N-94 and N-01 to provide a comprehensive description of the performance of the PET scanner in both brain- and whole-body-like conditions and in 2D and 3D acquisition modalities. The phantom filling procedure, the acquisition, the reconstruction and the data analysis protocol are described step by step.

The results of the physical characterisation are discussed below, parameter by parameter, with respect to the feasibility of the tests performed and the comparison between the N-94 and N-01 tests. Furthermore, the results obtained with the D-ST are compared with the performances of a widely used PET tomograph, the GE *Advance*, produced by the same manufacturer, with similar architecture but designed as a general-purpose machine to cover a wide range of applications (neurology and cardiology, besides oncology).

*Spatial resolution*

Spatial resolution was measured as the FWHM and FWTM of a line spread function and of a point spread

function in N-94 and N-01, respectively. While the N-94 spatial resolution test is very easy to perform, N-01 has the advantage of providing in a single measure both transverse and axial resolutions, but it is more difficult with regard to the practical preparation of the three point sources, which should be equal and very small (about 1 mm in the *x*, *y* and *z* directions).

Spatial resolution, on the order of 6.5 mm at 1 cm off centre, was slightly better in 2D than in 3D and slightly worse in the N-94 (LS function) than in the N-01 (PS function) test. Axial resolution was on the order of 5 mm (N-01).

In comparison with the *Advance* scanner (transverse and axial resolution both 5.1 mm, N-94 at 1 cm off centre), the crystal dimensions of the D-ST (D-ST: 6.3 mm×6.3 mm and *Advance*: 4.0 mm×8.0 mm) were such as to slightly sacrifice transverse resolution but improve axial sampling (half centre-to-centre crystal distance: 3.27 mm vs 4.25 mm) [16, 17]. The final axial resolution is influenced by the number of planes which contribute to the generation of direct and cross planes (five and six for the D-ST and three and four for the *Advance*).

### *Sensitivity*

Sensitivity is measured differently with N-94 and N-01. While N-94 measures the sensitivity of a PET system by using a cylindrical phantom filled with a known concentration of $^{18}$F in water, N-01 uses a thin, long LS (70 cm) filled with $^{18}$F contained within an aluminium housing to which successive aluminium sleeves, of known thickness, are added during the measurement. The N-01 test was developed with the aim of avoiding dependence of the sensitivity results on the different scatter correction techniques implemented by different scanner manufacturers [18]. On the other hand, measurement of the sensitivity by the N-01 test is very sensitive (particularly in 3D) to the exact filling of the LS over the 70 cm.

The D-ST has a high system sensitivity in both 2D and 3D. In 2D, the D-ST system sensitivity is about 40% higher than the sensitivity of the *Advance* PET system (8,567 cps/kBq/cc vs 6,162 cps/kBq/cc) [16], while the slice sensitivity is about the same (187 cps/kBq/cc vs 176 cps/kBq/cc for direct planes and 211 cps/kBq/cc vs 197 kcps/kBq/cc for cross planes, respectively) [16]. In 3D, the system sensitivity of the D-ST is 36,649 cps/kBq/cc, compared with 33,729 cps/kBq/cc for the *Advance* [17]. The high sensitivity of the D-ST in 2D mode is mainly due to the short length of the inter-plane septa (5.4 cm for D-ST vs 12.7 cm for the *Advance*), which also allows the bore of the system to be 70 cm as compared with 56 cm for the *Advance*. In 3D, the high sensitivity of the D-ST is due to the wide acceptance angle used in the acquisition configuration (a maximum delta plane of 23 for the D-ST vs 11 for the *Advance*). Furthermore, the D-ST has a smaller ring diameter (88.6 cm vs 92.7 cm), which also contributes to an increase in the sensitivity of the system.

### *Scatter fraction*

Scatter fraction (SF) is measured using an LS positioned at three different radial distances in a water-filled cylindrical phantom with the N-94 protocol, and using a long LS (70 cm) filled with $^{18}$F positioned in a 70-cm Teflon cylinder with the N-01. With the N-94, care must be taken to prepare an LS as long as the phantom and symmetrical in the axial FOV, in order to avoid asymmetries of the scatter function (in particular in 3D).

It should be noted that the phantom used in this work for the N-94 test had the LSs positioned at 0, 4 and 8 cm off centre, while the N-94 standard phantom has the LSs at 0, 4.5 and 9 cm off centre. This should not significantly change the value of the global scatter fraction, although hampering a direct comparison with scatter fraction values measured using the standard N-94 phantom.

Scatter fraction in 2D was 15% according to N-94 and 19% according to N-01. These values are in fact higher than that of the *Advance* (N-94: 9%), as a result of the short length of the inter-plane septa in the D-ST. A 15% scatter fraction is still low enough to be handled and corrected for by a post-processing scatter correction technique (see results in respect of scatter correction accuracy).

Scatter fraction in 3D was 30% according to N-94 and 45% according to N-01. Scatter fraction is lower in the D-ST than in the *Advance* (N-94: 36%), as a result of a higher low-energy threshold of the discrimination energy window (375 keV vs 300 keV). In fact, the improved electronics of the D-ST yield a mean energy resolution of 16–17% over the 10,080 detectors in the system, as compared with a system energy resolution of about 25% in the *Advance*.

Scatter fraction measured according to N-01 is higher than that measured according to N-94, as a result of the contribution of radioactivity from outside the FOV, which is taken into account by the N-01 protocol, using 70-cm-long phantoms.

### *Count rate performances*

Count rate tests are performed with N-94 by using a cylindrical phantom filled with a known concentration of $^{18}$F in water, while N-01 uses the same phantom as for the SF test. SF and count rate losses are in fact part of the same measure in N-01.

Comparison of the count rate performance assessed by N-94 and N-01 is difficult owing to the different experimental conditions. In general, the D-ST system showed very good count rate performance in both 2D

and 3D mode. This is proved by a comparison with the performance of the *Advance* scanner, e.g. N-94 3D NEC rate peak: 270 kcps at 34.38 kBq/cc vs 200 kcps at about 20 kBq/cc (from Fig. 7, reference [17]); 50% dead time: 834 kcps at 53 kBq/cc vs 550 kcps at 31.5 kBq/cc (from Fig. 7, reference [17]).

As a result of the *k* value used in the calculation of the NEC rate, the NEC($k$=1) curve is higher than the NEC($k$=2) curve. These N-01 NEC curves confirm the high count rate performances of the D-ST, in particular in 3D, where the NEC curves show the peak of the system response at activities used for clinical studies. In fact, the NEC peaks are reached at activity concentrations of about 14.86 kBq/cc and 10.84 kBq/cc, respectively. It is to be noted that the range of activity concentrations in clinical FDG studies corresponds to that at which the NEC curves reach the maximum values.

With both N-94 and N-01, the correction for count rate losses is accurate. As an example, in 3D, the N-01 error was less than 2% at the peak NEC rate curve.

### *Scatter and attenuation correction accuracy*

While N-94 has two specific tests to evaluate the accuracy of scatter and attenuation correction (AC) techniques implemented in the system, N-01 uses a single parameter within the IQ test to simultaneously evaluate both corrections (residual error in the lung region). In general, scatter and attenuation corrections have some degree of inter-dependence and the contribution of the individual correction procedure is hardly distinguished. In fact, in the event of an inaccurate scatter correction, the residual scatter component would be improperly corrected for attenuation.

In a PET/CT system, AC is performed after conversion of the Hounsfield numbers of the CT image to attenuation coefficients for the 511 keV of the annihilation events. The conversion law used in the D-ST is based on a bilinear transformation, which is obtained using three reference points for air, water and bone [19, 20].

In the N-94 2D scatter correction accuracy test, the residual error was very low, as a result of the appropriateness of the scatter correction model and of the controlled experimental conditions (a simple cylindrical phantom filled with radioactive water), thus implying a simple transformation from water Hounsfield number to 511-keV attenuation coefficient. In 3D, the negative error found indicates an over-estimation of the scatter component. The N-94 AC accuracy test shows that the residual errors for two of the three inserts (air and water) were low. In fact, air and water are materials on which the conversion law from Hounsfield numbers to 511-keV attenuation coefficients is based. For the third insert (Teflon), the error was significantly higher. As already reported in the Results section, Teflon is not an appropriate bone-equivalent material and AC is affected by an incorrect transformed attenuation coefficient.

In the N-01 test, scatter and AC accuracy were evaluated on a low-density (polystyrene) cold activity region simulating the human lungs. The residual error was 23.5% and 16.5% in 2D and 3D, respectively. These errors could mainly derive from an inaccurate attenuation coefficient conversion law for the low-density material simulating the lungs.

The scatter and AC errors also depend on the reconstruction algorithm used and, in the case of an iterative algorithm, on the number of iterations.

### *Image quality*

Image quality (IQ) represents a new feature of the N-01 protocol (not present in the N-94 protocol), designed to assess the overall performance of a PET system on the basis of a visual inspection of the final reconstructed images of a phantom simulating hot and cold lesions in the thorax. In fact, the results of the IQ test are dependent on the operator skill during the phantom filling procedure and also on the reconstruction protocol used (algorithm and parameters).

The results of this test presented in Table 6 and Fig. 9 show a slightly better hot sphere recovery in 2D than in 3D, while cold contrast is higher in 3D than in 2D. The background variability is lower in 3D, as is the residual error in the lung region. Both of the reconstruction protocols considered use an iterative reconstruction algorithm (OSEM in 2D mode and FORE-WLS in 3D) with a low number of iterations. In a clinical implementation, besides reconstruction time considerations, the need to maintain the noise in the reconstructed images at a low level usually inhibits the use of a higher number of iterations, which, on the other hand, would be needed to allow the convergence of iterative algorithms particularly in regions of low activity. For instance, the use of one more iteration in the 2D reconstruction protocol would have improved the results obtained for both the hot recovery coefficient (by a factor of up to 30% for the smallest sphere) and the cold contrast (by a factor of about 13%), with a smaller residual error in the “lung” region but an increase in the background variability.

### *Conclusion*

In conclusion, the new fully integrated Discovery ST shows good overall performances in both 2D and 3D as a result of an optimised scanner design. This yields a balanced performance of the several physical parameters influencing the final image quality. In particular, high sensitivity results in low statistical noise and the consequent recovery of spatial resolution in clinical studies. Furthermore, the good NEC response allows clinical studies to be optimised in terms of the signal to noise ratio.

*Acknowledgements*. This work was in part supported by a research grant (FIRB N. RBNE015AKZ_001) from the Italian Ministry of Education, University and Research (MIUR).

## References


1. Jerusalem G, Hustinx R, Beguin Y, Fillet G. PET scan imaging in oncology. Eur J Cancer 2003; 39:1525–1534.
2. Hutton BF, Braun M, Thurfjell L, Lau DY. Image registration: an essential tool for nuclear medicine. Eur J Nucl Med Mol Imaging 2002; 29:559–577.
3. Townsend DW, Beyer T, Blodgett TM. PET/CT scanners: a hardware approach to image fusion. Semin Nucl Med 2003; 33:193–204.
4. Beyer T, Townsend DW, Brun T, et al. A combined PET/CT tomograph for clinical oncology. J Nucl Med 2000; 41:1369–1379.
5. Beyer T, Townsend DW, Blodgett TM. Dual-modality PET/CT tomography for clinical oncology. Q J Nucl Med. 2002; 46: 24–34.
6. Messa C, Bettinardi V, Picchio M, Pelosi E, Landoni C, Gianolli L, Gilardi MC, Fazio F. PET/CT in diagnostic oncology. Q.J Nucl Med 2004:in press.
7. Humm JL, Rosenfeld A, Del Guerra A. From PET detectors to PET scanners. Eur J Nucl Med Mol Imaging 2003; 30: 1574–1597.
8. Perez CA, Bradley J, Chao CK, Grisby PW, Mutic S, MalyapaR. Functional imaging in treatment planning in radiation therapy: a review. Rays 2002; 27:157–173.
9. Mawlawi O, Kolmyer SG, Williams JJ, Stearns CW, Culp RF, Podoloff DA, Macapinlac H. Performance characteristics of the GE Discovery ST PET/CT scanner using the NEMA NU-2 standard. Proceedings of the SNM 50th Annual Meeting, J Nucl Med Suppl 2003; 44:111P.
10. Turkington TG, Kolmyer SG, Stearns CW, Williams JJ, Hawk TC. Characterization of the Discovery ST and *Advance* PET systems using a whole-body phantom. Proceedings of the SNM 50th Annual Meeting, J Nucl Med Suppl 2003; 44:111P.
11. Karp JS, Daube-Witherspoon ME, Hoffman EJ, Lewellen TK, Links JM, Wong WH, Hichwa RD, Casey ME, Colsher JG, Hitchens RE, Muehllehner G, Stoub EW. Performance standards in positron emission tomography. J Nucl Med 1991; 32:2342–2350.
12. National Electrical Manufacturers Association. NEMA NU-2 Standards Publication NU-2-1994: performance measurements of positron emission tomography. Washington DC: National Electrical Manufacturers Association, 1994.
13. National Electrical Manufacturers Association. NEMA NU-2 Standards Publication NU-2-2001: performance measurements of positron emission tomography. Rosslyn, VA: National Electrical Manufacturers Association, 2001.
14. Daube-Witherspoon ME, Karp JS, Casey ME, DiFilippo FP, Hines H, Muehllehner G, Simcic V, Stearns CW, Adam LE, Kolmyer S, Sossi V. PET performance measurements using the NEMA NU 2-2001 standard. J Nucl Med 2002; 43:1398–1409.
15. Burger C, Goerres G, Schoenes S, Buck A, Lonn AHR, von Schulthess GK. PET attenuation coefficients from CT images: experimental evaluation of the transformation of CT into PET 511-keV attenuation coefficients. Eur J Nucl Med 2002; 29:922–927.
16. DeGrado RT, Turkington GT, Williams JJ, Stearns CW, Hoffman JM, Coleman ER. Performance characteristics of a whole body PET scanner. J Nucl Med 1994; 35:1398–1406.
17. Lewellen TK, Kolmyer SG, Miyaoka RS, Kaplan MS. Investigation of the performance of General Electric *Advance* positron emission tomograph in 3D mode. IEEE Trans Nucl Sci 1996; 43:2199–2206.
18. Bailey DL, Jones T, Spinks TJ. A method for measuring the absolute sensitivity of positron emission tomographic scanners. Eur J Nucl Med 1991; 18:374–379.
19. Nakamoto Y, Osman M, Cohade C, Marshall LT, Jonathan ML, Kolmyer S, Richard L, Wahl L. PET/CT: comparison of quantitative tracer uptake between germanium and CT transmission attenuation-corrected images. J Nucl Med 2002; 43: 1137–1143.
20. Burger C, Goerres G, Schoenes S, Buck A, Lonn AHR, von Schulthess GK. PET attenuation coefficients from CT images: experimental evaluation of the transformation of CT into PET 511 keV attenuation coefficients. Eur J Nucl Med Mol Imaging 2002; 29:922–927.